Long-Lived Phonon Polaritons in Hyperbolic Materials

Guangxin Ni,* Alexander S. McLeod, Zhiyuan Sun, Joseph R. Matson, Chiu Fan Bowen Lo, Daniel A. Rhodes, Francesco L. Ruta, Samuel L. Moore, Rocco A. Vitalone, Ramon Cusco, Luis Artús, Lin Xiong, Cory R. Dean, James C. Hone, Andrew J. Millis, Michael M. Fogler, James H. Edgar, Joshua D. Caldwell, and D. N. Basov*

Read Online

ACCESS | Metrics & More | Article Recommendations | Supporting Information

ABSTRACT: Natural hyperbolic materials with dielectric permittivities of opposite signs along different principal axes can confine long-wavelength electromagnetic waves down to the nanoscale, well below the diffraction limit. Confined electromagnetic waves coupled to phonons in hyperbolic dielectrics including hexagonal boron nitride (hBN) and α-MoO_3 are referred to as hyperbolic phonon polaritons (HPPs). HPP dissipation at ambient conditions is substantial, and its fundamental limits remain unexplored. Here, we exploit cryogenic nanoinfrared imaging to investigate propagating HPPs in isotopically pure hBN and naturally abundant α-MoO_3 crystals. Close to liquid-nitrogen temperatures, losses for HPPs in isotopic hBN drop significantly, resulting in propagation lengths in excess of 8 μm, with lifetimes exceeding 5 ps, thereby surpassing prior reports on such highly confined polaritonic modes. Our nanoscale, temperature-dependent imaging reveals the relevance of acoustic phonons in HPP damping and will be instrumental in mitigating such losses for miniaturized mid-infrared technologies operating at liquid-nitrogen temperatures.

KEYWORDS: *phonon polaritons, hyperbolic materials, nanoinfrared imaging, van der Waals heterostructures*
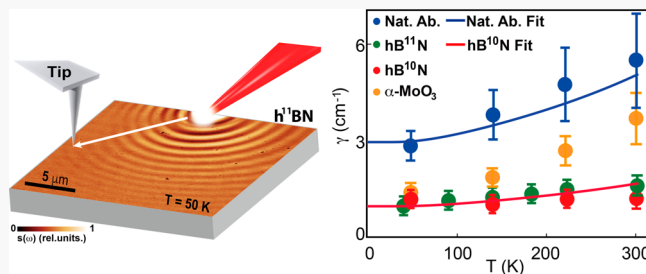
We investigate hyperbolic phonon polariton (HPP) propagation and dissipation in isotopically pure hexagonal boron nitride (h¹⁰BN, h¹¹BN), along with naturally abundant hBN and α-MoO_3 van der Waals crystals using near-field infrared (IR) microscopy. Nano-IR methods allow one to directly visualize polaritonic standing waves on the surfaces of these hyperbolic materials.[1−7] Similar to graphene plasmon polariton investigations,[8−13] both the wavelength of the HPP $\lambda_p(\omega)$ and its dissipation γ can be readily obtained from nano-IR images (Figures 1 and 2), with these two quantities allowing one to extract the complex dielectric function $\varepsilon(\omega) = \varepsilon' + i\varepsilon''$ of a phononic medium.[3−6] Earlier attempts have characterized HPPs in isotopically pure hBN (h¹⁰BN, h¹¹BN) and in α-MoO_3 crystals at ambient conditions.[6,14−19] However, the fundamental limits of HPP dissipation and lifetime remain to be determined as this necessarily relies on temperature-dependent nanoimaging of polaritonic waves. In this work, we report cryogenic nanoimaging results of these van der Waals materials for the first time, demonstrating record-long HPP lifetimes. We studied isotopically pure hBN and biaxial hyperbolic α-MoO_3 crystals and compared these results with naturally abundant hBN crystals. Combined with theoretical models, we examined the physics governing HPP dissipation in isotopically pure hyperbolic crystals.
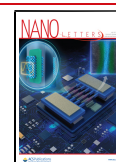
To perform cryogenic nanoimaging, we utilized a home-built scanning near-field IR microscope operating at variable temperatures.[8,20−22] In this setup, the incident light with IR frequency ω is focused onto the metallized tip of an atomic force microscope (AFM). As the tip approaches the sample, a concentrated evanescent field excites polaritonic modes with a $\lambda_p(\omega)$ that is much shorter than the free-space wavelength $\lambda_{IR} = 2\pi c/\omega$ of the incident photons.[23−27] This unique nano-IR apparatus has been routinely employed in studies of plasmon and phonon polaritons as well as for visualizing inhomogeneities in complex oxides.[20−22] In the previous HPP nanoimaging studies, a physical sample edge was chosen as the HPP wave reflector,[6] resulting in the imaging of coexisting fringes with two distinct periodicities λ_p and $\lambda_p/2$. To avoid the complications of λ_p and $\lambda_p/2$ fringe decompositions, an alternative approach is preferred. In our device (Figure 1b), prepatterned micron-sized Au disk structures residing on top of the hBN crystals (bottom of α-MoO_3) serve as fixed HPP antennas (Figures 1 and 2) predominantly producing fringes with λ_p periodicity.

a

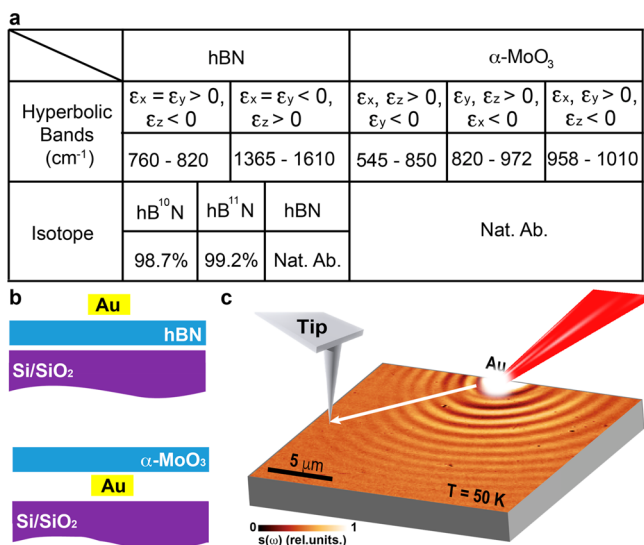|	hBN		α-MoO₃		
	$\varepsilon_x = \varepsilon_y > 0$, $\varepsilon_z < 0$	$\varepsilon_x = \varepsilon_y < 0$, $\varepsilon_z > 0$	$\varepsilon_x, \varepsilon_z > 0$, $\varepsilon_y < 0$	$\varepsilon_y, \varepsilon_z > 0$, $\varepsilon_x < 0$	$\varepsilon_x, \varepsilon_y > 0$, $\varepsilon_z < 0$
Hyperbolic Bands (cm⁻¹)	760 - 820	1365 - 1610	545 - 850	820 - 972	958 - 1010
Isotope	hB¹⁰N	hB¹¹N	hBN	Nat. Ab.		
	98.7%	99.2%	Nat. Ab.			

b

c

Figure 1. Nano-IR imaging of phonon polaritons in hyperbolic structures at cryogenic temperatures. (a) Table with properties of examined hyperbolic materials. The listed hyperbolic bands are for naturally abundant hBN and α-MoO₃. (b) Sketch of the layered Au/hBN and α-MoO₃/Au structures. The lithographically defined gold (Au) microstructures on top of the hBN (or below the α-MoO₃) serve as effective polaritonic launchers. (c) Nanoscale infrared image of phonon polariton fringes from the Au/h¹¹BN, expressed by the normalized scattering amplitude s acquired at a temperature of $T = 50$ K. The arrows represent the propagation direction of the polaritonic waves. These experiments simultaneously visualize the local electric field associated with interference fringe patterns from phonon polaritons launched by the Au microstructures.

We begin with a survey of a large-area (25×20 μm²) image of HPP standing waves in h¹¹BN obtained at $T = 50$ K (Figure 1c) with an IR laser operating at $\lambda_{IR} = 6.6$ μm. Here we display raw data in the form of the scattered near-field amplitude s normalized to the corresponding signal detected from the gold disks, whose optical response provides a convenient temperature (T)-independent reference. The most prominent aspect of the image in Figure 1c is that the entire field of view is filled with HPP fringes. As expected, the λ_p-fringes dominate the field of view, emanating from the Au antenna and propagating radially outward. Even a cursory inspection of Figure 1c reveals that HPPs remain confined with $\lambda_{IR}/\lambda_p > 5$, and yet, they travel over tens of microns, far exceeding previous measurements at ambient temperature.[6,14]

Nano-IR data in Figure 2 attest to a clear reduction of HPP losses in monoisotopic hBN specimens at lower temperatures with the incident frequency of 1522 cm⁻¹ (6.57 μm). HPPs in h¹¹BN films (thickness of 180 nm) at room temperature exhibit 5 μm propagation lengths ($L_p = 1/(2\text{Im}\{q_p\})$, where $q_p = q_p' + iq_p''$, see below), corresponding to quality factor $Q_p \sim 35$ as defined below (Figure 2d,e). As the temperature is reduced, we observe a systematic increase in quality factor and propagation length. Specifically, at $T = 45$ K, Q_p exceeds 60, which represents the highest quality factor achieved to date. To elucidate the underlying polariton scattering mechanisms, we have also performed T-dependent studies in h¹⁰BN and naturally abundant samples for systematic comparisons (Figure 2a,c). Two observations can be drawn. First, we observed that the monoisotopic specimens of h¹⁰BN and h¹¹BN share nearly identical propagation lengths at all temperatures. These HPP oscillations exhibit scattering lifetimes 2−3 times longer than

those observed in naturally abundant hBN crystals, consistent with prior results.[6] Second, HPP propagation lengths at a given frequency generally increase with reduced temperatures for all hBN specimens, as documented in Figure 2d,e. Notably, we found that both h¹⁰BN and h¹¹BN exhibit different temperature dependences compared with naturally abundant hBN crystals of similar thickness, as manifested by their HPP oscillations and the quality factor Q_p (Figure 2d,e). These overall trends suggest different underlying mechanisms of phonon scattering between isotopically pure and naturally abundant hBN, as discussed in the following sections in detail.

We have also investigated the temperature dependence of hyperbolic HPP in exfoliated crystals of α-MoO₃, a natural material that exhibits in-plane hyperbolicity at mid-IR frequencies, to determine if the same temperature-dependent scattering is observed as in hBN.[14,15,17] In contrast to the convex wavefronts in isotropic materials, concave wavefronts of the HPP modes in thin slabs of α-MoO₃ have been observed at ambient conditions.[14,15,17,18] In Figure 3, we show raster scans of an α-MoO₃ crystals (∼200 nm thickness) exfoliated onto an Au antenna obtained at temperatures ranging from 50 to 300 K and at the frequency of 928 cm⁻¹. At room temperature, HPP interference fringes with concave shapes along the (100) direction were observed, consistent with the isofrequency curves as expected from the in-plane hyperbolic responses.[14,15,17] As the temperature is reduced, we observe a systematic increase in both the overall propagation distance and the number of detectable HPP oscillations, consistent with hBN results. The damping rate in α-MoO₃ is lower across temperatures than in natural hBN, while slightly higher than in monoisotopic hBN. At $T = 50$ K, HPP oscillations approach propagation lengths of 20 μm (Figure 3a). Similar temperature dependence of HPP was also detected in the elliptical response regime (see Supporting Information). These overall trends are similar to our results on hBN isotopes, indicating the uniform characteristics of phonon propagation and dissipation emerging at low temperatures in hyperbolic crystals.

To quantify the dynamics underlying the propagation of HPPs in hBN and α-MoO₃ crystals, we present an analysis based on the complex momentum of the polariton $q_p = q_p' + iq_p''$. The real part defines the wavelength through $\lambda_p = 2\pi/q_p'$, whereas the imaginary part q_p'' quantifies dissipation and the quality factor $Q_p = q_p'/q_p''$. To quantify Q_p, we fit the oscillating line-profiles away from the Au antenna employing the spheroidal model with an analytical formula of $S(x) = \frac{A\sin(q_p' x + B)e^{-q_p'' x}}{\sqrt{x + \zeta}}$, with complex parmters q_p and real A, B, and ζ as fitting parameters[26] (see Supporting Information for details). This analytical formula accounts for fringe decay processes away from the antenna with the presence of a finite damping ($q_p'' > 0$) and a geometric spreading term in the denominator. As shown by solid curves superimposed on polariton line-profiles in Figure 2d and Figure 3b, the fitted results match well with the experimental data across variable temperatures. This analysis allowed us to extract the temperature-dependent quality factors $Q_p (T)$ for polaritons in all isotopes of hBN and α-MoO₃ crystals for the first time, as presented in Figure 2e and Figure 3c. Specifically, we found the highest quality factor $Q_p (T) > 60$ in near-monoisotopic hBN flakes at cryogenic temperatures.

We now outline the damping rate analysis based on the temperature-dependent results extracted from hBN crystals. In Figure 4, we plot the temperature-dependent HPP damping
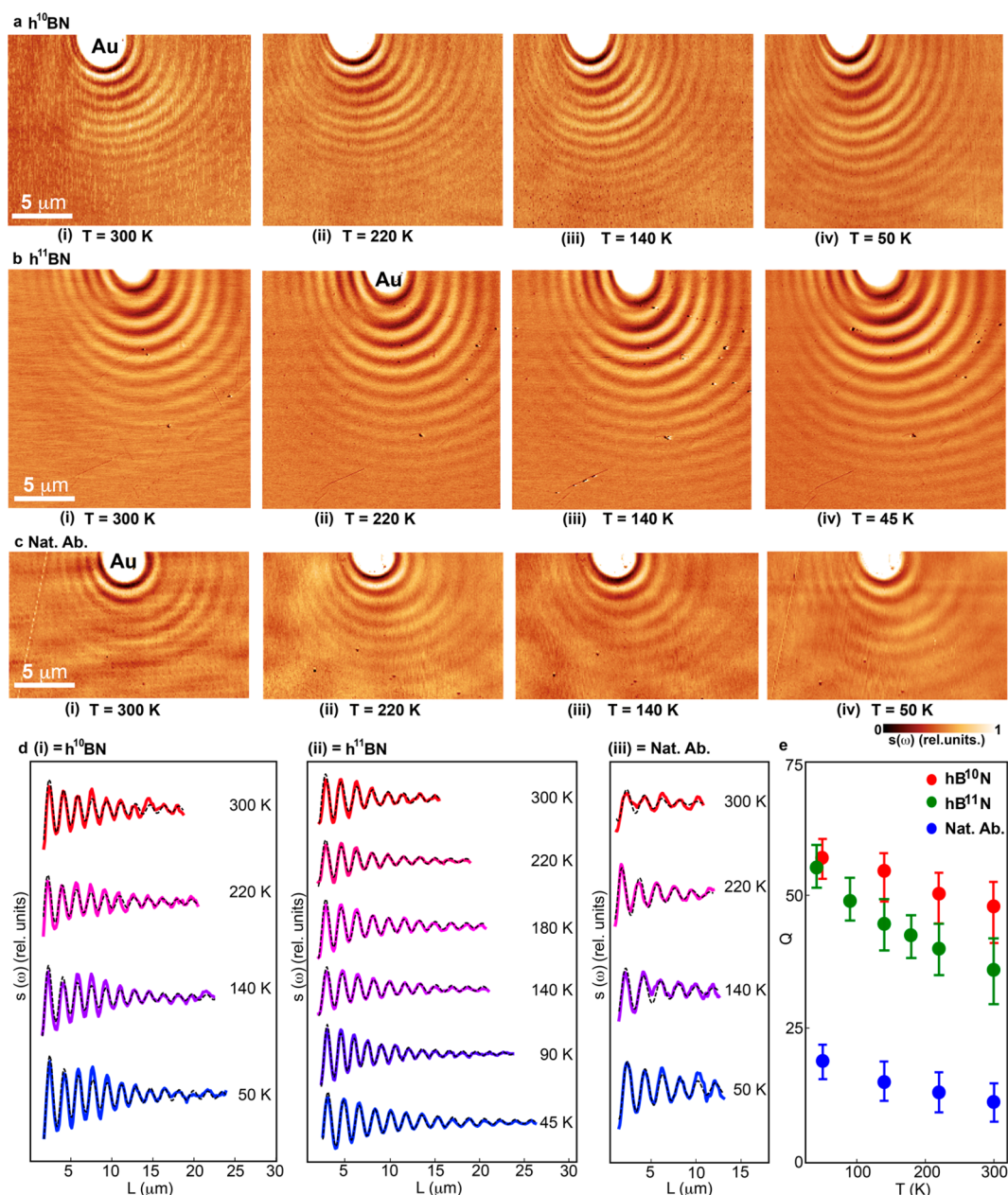
Figure 2. Temperature dependence of phonon polariton propagation in isotopic hBN devices. (a−c) Nano-IR images of the normalized scattering amplitude s acquired at sequential sample temperatures from $h^{10}BN$, $h^{11}BN$, and naturally abundant hBN, respectively. A gold disk (labeled Au) functions as an antenna that launches hBN phonon polariton waves. (d) Line profiles of phonon polariton fringes propagating from left to right, as a function of the distance L from the gold launcher. The variable attenuation of the propagating waveform (solid curves) is characteristic of the temperature-dependent phonon polariton damping rate. Dash-dotted lines are fittings of the wave profile using damped sinusoidal functions corrected by geometric decaying factors (see main text and Supporting Information). (e) The temperature dependence of the quality factor Q_p for phonon polariton waves obtained from nanoscale infrared images shown in panels a−d. The thickness of $h^{10}BN$, $h^{11}BN$, and naturally abundant hBN flakes are 150, 200, and 180 nm, respectively.

rates (line width) $\gamma(T) = \omega v_g/(Q_p(T)v_p)$ converted from quality factors, where v_g and v_p are the group and phase velocities of the modes. Note that the damping rates are on the order of several wavenumbers (approaching $\omega/1000$), while the quality factors defined in terms of momenta are relatively small due to the very low group-phase velocity ratio: $\frac{v_g}{v_p} \sim 0.04$ (obtained from theoretical HPP dispersions, see Supporting Information). Several pieces of information arise from Figure 4. First, the HPP damping rates scale quasi-linearly with temperature for all samples. This is different from the

nonlinear temperature dependence of plasmon damping rates observed in pristine graphene.[8] Second, compared to $h^{11}BN$ and $h^{10}BN$, the polariton damping rate in naturally abundant hBN displays a higher residual damping in the zero-Kelvin limit and a steeper slope to the temperature dependence.

The temperature-dependent studies offer insights into the damping mechanisms of HPP in both hBN and α-MoO_3 crystals. We posit that the temperature dependence can only be described by the participation of acoustic phonons in the scattering process, as the optical phonons are not thermally occupied in the temperature range of $T < 300\ K = 208\ cm^{-1}$
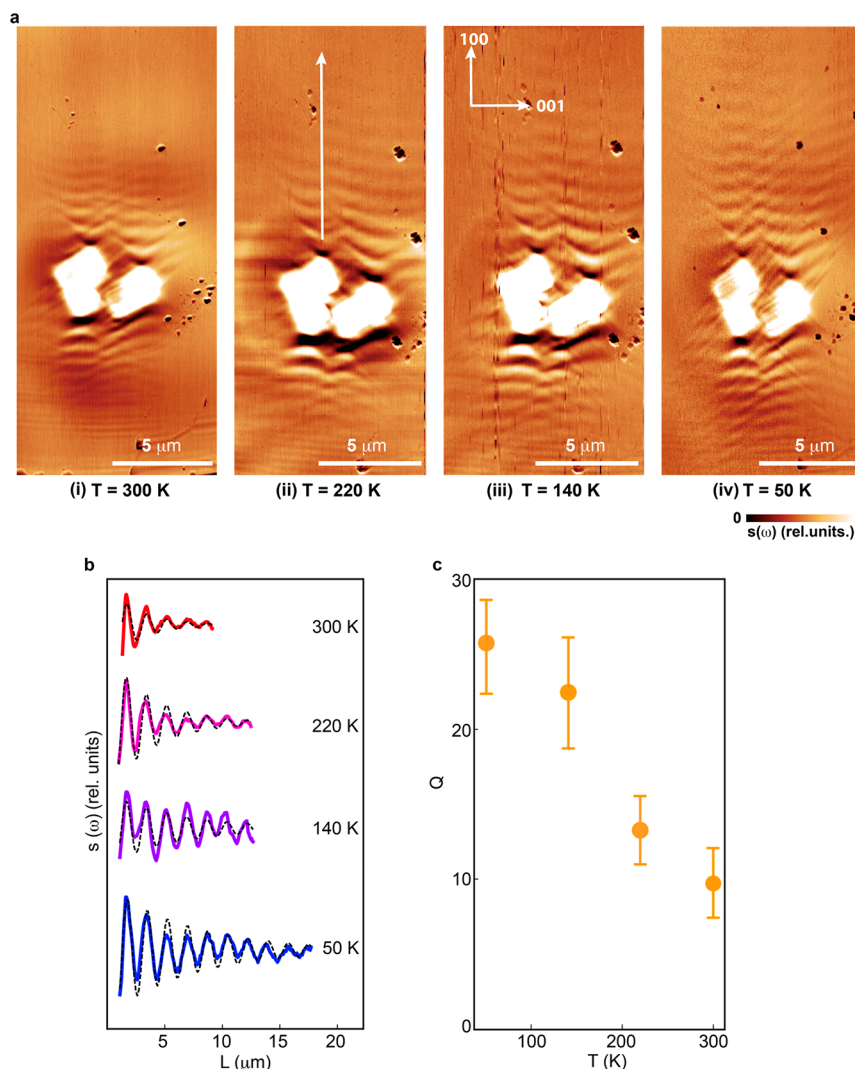
Figure 3. Temperature dependence of phonon polariton propagation in α-MoO$_3$ crystals. (a) Nano-IR images of the normalized near-field scattering amplitude s acquired at sequential sample temperatures from α-MoO$_3$ crystals. A pair of gold disks beneath the α-MoO$_3$ crystal function as antennas that launch polaritonic waves. The white arrow indicates the location of extracted line profiles of phonon polaritons. (b) Line profiles of phonon polariton fringes propagating from left to right, as a function of the distance L from the gold launcher. Dash-dotted lines represent the results of numerical simulations performed to identify the temperature dependence of the complex phonon polariton wavevector and associated damping rate (see main text and Supporting Information). (c) Temperature dependence of the quality factor Q_p of phonon polariton waves obtained from nanoscale infrared images shown in panel a.

(see Supporting Information). In isotopically pure hBN, we attribute the leading damping channel to momentum relaxation caused by acoustic phonons, that is, the polariton being scattered from its initial state with momentum k_i to the final state with momentum $k_f = k_i + q$ by absorbing/emitting an acoustic phonon with momentum $\pm q$ (Figure 4b). Under reasonable approximations (see Supporting Information, section 4.1), the resulting scattering rate reads $\gamma_a(\omega, T) \sim \gamma_{a0}(\omega)f\left(\frac{T}{T_\Lambda}\right)$, where $\gamma_{a0}(\omega)$ is a characteristic scattering rate, $T_\Lambda = v_a\Lambda/k_B$ is a temperature "cutoff", v_a is the speed of acoustic phonons, and Λ is the momentum cutoff of the hyperbolic polaritons. The temperature dependence is captured by the scaling function $f\left(\frac{T}{T_\Lambda}\right)$, which behaves as $1 + \frac{8\pi^4}{15}\left(\frac{T}{T_\Lambda}\right)^4$ when $T \ll T_\Lambda$ and as $1 + \frac{8}{3}\frac{T}{T_\Lambda}$ when $T \gg T_\Lambda$.

Isotopic impurities in natural hBN can also induce the same decay process as acoustic phonons, giving rise to a temperature-independent scattering rate $\gamma_i(\omega)$. Both $\gamma_i(\omega)$ and $\gamma_{a0}(\omega)$ are proportional to the polariton density of states $D(\omega) = \partial_\omega\sqrt{-\frac{\epsilon_x}{\epsilon_z}}$, where ϵ_x and ϵ_z are the in-plane/out-of-plane dielectric functions of hBN. Here $D(\omega)$ diverges as $\frac{1}{(\omega - \omega_{TO})^{3/2}}$ when the frequency approaches the transverse optical (TO) phonon, while weakly depending on $\frac{1}{(\omega_{LO} - \omega)^{1/2}}$ as the frequency approaches the longitudinal optical (LO) phonons. Such a strong frequency dependence suggests that the frequency-dependent damping rate $\gamma(\omega)$ needs to replace its constant counterpart in the Lorentzian oscillator model. Note that polaritons with frequency ω can also decay into E_{1u} TO phonons or E_{2g} phonons (nearly flat dispersion at the frequency $\omega_{TO} = \omega_g = 1360$ cm^{-1}) by emitting an acoustic phonon. This contributes to a scattering rate $\gamma_g(\omega,T) =$
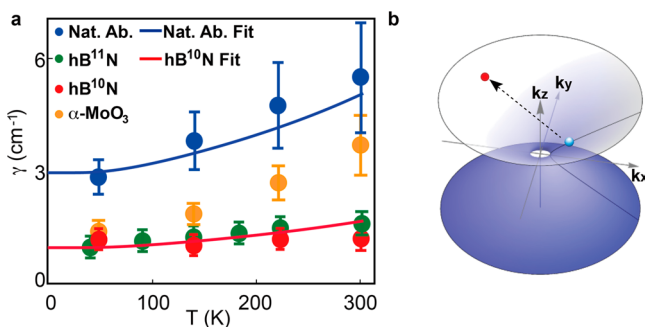
Figure 4. Theoretical modeling of phonon polariton damping rate γ in hyperbolic crystals. (a) The dots corresponding to the extracted dissipation factors as a function of temperature; the solid blue and red lines are the theoretical fitting results as detailed in the main text. The parameters used here are $hB^{11}N$: $\omega = 1522$ cm^{-1}, $v_g/v_p = 0.037$; $hB^{10}N$: $\omega = 1553$ cm^{-1}, $v_g/v_p = 0.039$; naturally abundant hBN: $\omega = 1522$ cm^{-1}, $v_g/v_p = 0.039$; B^{11}: α-MoO$_3$ = 928 cm^{-1}, $v_g/v_p = 0.039$. The group and phase velocity in α-MoO$_3$ are taken from ref 14. (b) The illustration of scattering of a hyperbolic polariton from an initial state (blue dot) to a final state (red dot) on the iso-frequency surface by either emitting/obsorbing an acoustic phonon or by impurity potential.

$\gamma_{g_0}(\omega)(n_b(\omega - \omega_{TO}) + 1)$ where the boson occupation number n_b gives the temperature dependence and γ_{g_0} is a frequency scale depending on ω. However, our theoretical modeling suggests that this term is negligibly small (see Supporting Information, section 4). The functional forms of γ_a, γ_i, and γ_g, therefore, represent these new results.

The steeper temperature-dependence of damping rate in natural hBN implies a higher-order decay channel involving both impurities and acoustic phonons, which we subsume by $\gamma_h(T) = \kappa_i(\omega)(\gamma_a(\omega,T) + \gamma_g(\omega,T))$ (see Supporting Information). The total polariton damping rates for natural and isotopically pure hBN are thus

$$\gamma_{iso}(T) = \gamma_0 + \gamma_a(T) + \gamma_g(T) \text{ and } \gamma_{nat}(T)$$

$$= \gamma_{iso}(T) + \gamma_i + \gamma_h(T)$$

where γ_0 is a temperature-independent scattering rate due to other decay processes.[28,29] The dashed fitting lines in Figure 4 correspond to $\gamma_0 = 0.4$ cm^{-1}, $\gamma_{a_0} = 0.6$ cm^{-1}, $\gamma_{g_0} = 0$, $\gamma_i = 0.5$ cm^{-1}, $\kappa_i = 2.5$, and $T_\Lambda = 450$ K. Note that these fitting parameters are obtained for our simplified analytical model. Further dedicated first-principle calculations are possibly needed for fine-tuning, which is beyond the scope of the current work. On top of the above intrinsic damping channels, the dielectric loss from the SiO$_2$ substrate contributes <20% to the total damping rate at the experimental frequency of 1522 cm^{-1}.

In summary, our results account for HPP dynamics in high-quality hyperbolic crystals. Quality factors and scattering rates of hyperbolic polaritons in naturally abundant and mono-isotopic hBN, as well as α-MoO$_3$, have been extracted from cryogenic nanoimaging studies. Though limited by acoustic phonon scattering and other decay channels, the HPP propagation length and lifetime in monoisotopic hBN at low-T exceed 8 μm and 5 ps, a new record among all-natural hyperbolic materials reported so far. Our first report of HPP nanoimaging studies of high-quality hyperbolic crystals at cryogenic temperatures demonstrates promising opportunities

for the exploration of advanced phononic switching,[30] polariton periodic orbits in cavities,[31] and nonlinear phenomena[32] in ultrapure polar samples at technologically relevant liquid nitrogen temperatures. Long-lived polaritons are of interest for applications in infrared signal processing, nano-photonic circuits, nanolight sensing and communications, as well as heat management at the nanoscale.[14,18]

Methods. *1. Sample Growth and Device Fabrication.* hBN crystals with the natural distribution of isotopes (20% B-10 and 80% B-11) were produced using a hot-pressed boron nitride ceramic boat, which served as both the container for the metal flux and as the B and N sources. For B^{10} and B^{11}-enriched hBN crystal growth, the procedure is modified to use elemental boron as a source material. Therefore, the boron nitride boat was replaced with an alumina crucible. High-purity 10B (99.22%) or 11B (99.41%) powders were mixed with Ni and Cr powders to give overall concentrations of 4% B, 48% Ni and 48% Cr. In this case, all nitrogen in the hBN originated from the flowing N$_2$ gas. Other than these changes, the procedure was the same as described above. The hBN crystals were then transferred onto SiO$_2$/Si substrates using the mechanical exfoliation method. After identifying the crystal thickness and uniformity, standard E-beam lithography is utilized to define Au launchers, followed by thermal annealing processes to remove contaminated polymer residuals.

2. Cryogenic IR Nanoimaging Experiments. IR nano-imaging experiments were performed using a home-built scattering-type scanning near-field optical microscope (s-SNOM) operating with variable sample temperatures from 50−300 K. All measurements are conducted under ultrahigh vacuum conditions at pressured <10^{-9} mbar to prevent sample surface contamination. The cryogenic s-SNOM is equipped with continuous-wave mid-IR quantum cascade lasers (day-lightsolutions.com) and CO$_2$ lasers (accesslaser.com). The s-SNOM is based on an atomic force microscope (AFM), operated for the present experiments in noncontact mode using cantilevered metallic AFM probes with tip apex radius ~25 nm and tapping frequencies ~270 kHz. A pseudoheter-odyne interferometric detection module is implemented in our s-SNOM to extract both scattering amplitude s and phase of the near-field signal. In the current work, we discuss only the former. In order to suppress background contributions to the backscattered near-field signal, we demodulated the detected signal at the third harmonic of the probe tapping frequency.

■ ASSOCIATED CONTENT

SI Supporting Information

The Supporting Information is available free of charge at https://pubs.acs.org/doi/10.1021/acs.nanolett.1c01562.

> Detailed description of the device fabrication and characterization, spheroidal modeling of the near field signal, dispersion of hyperbolic phonon polaritons, and discussion of the phonon polariton damping rate (PDF)

■ AUTHOR INFORMATION

Corresponding Authors

Guangxin Ni − *Department of Physics, Florida State University, Tallahassee, Florida 32306, United States; National High Magnetic Field Laboratory, Florida State University, Tallahassee, Florida 32310, United States;* ● orcid.org/0000-0002-7216-1829; Email: guangxin.ni@magnet.fsu.edu

D. N. Basov − *Department of Physics, Columbia University, New York 10027, United States*; Email: db3056@columbia.edu

Authors

Alexander S. McLeod − *Department of Physics, Columbia University, New York 10027, United States*

Zhiyuan Sun − *Department of Physics, Columbia University, New York 10027, United States*

Joseph R. Matson − *Department of Mechanical Engineering, Vanderbilt University, Nashville, Tennessee 37235, United States*

Chiu Fan Bowen Lo − *Department of Physics, Columbia University, New York 10027, United States*

Daniel A. Rhodes − *Department of Mechanical Engineering, Columbia University, New York 10027, United States;* orcid.org/0000-0002-7651-3211

Francesco L. Ruta − *Department of Physics and Department of Applied Physics and Applied Mathematics, Columbia University, New York 10027, United States;* orcid.org/0000-0002-8746-9420

Samuel L. Moore − *Department of Physics, Columbia University, New York 10027, United States*

Rocco A. Vitalone − *Department of Physics, Columbia University, New York 10027, United States*

Ramon Cusco − *Lluís Solé i Sabarís s.n., GEO3BCN-CSIC, 08028 Barcelona, Spain;* orcid.org/0000-0001-9490-4884

Luis Artús − *Lluís Solé i Sabarís s.n., GEO3BCN-CSIC, 08028 Barcelona, Spain*

Lin Xiong − *Department of Physics, Columbia University, New York 10027, United States*

Cory R. Dean − *Department of Physics, Columbia University, New York 10027, United States*

James C. Hone − *Department of Mechanical Engineering, Columbia University, New York 10027, United States*

Andrew J. Millis − *Department of Physics, Columbia University, New York 10027, United States*

Michael M. Fogler − *Department of Physics, University of California, San Diego, La Jolla, California 92093, United States*

James H. Edgar − *Tim Taylor Department of Chemical Engineering, Kansas State University, Manhattan, Kansas 66506, United States;* orcid.org/0000-0003-0918-5964

Joshua D. Caldwell − *Department of Mechanical Engineering, Vanderbilt University, Nashville, Tennessee 37235, United States;* orcid.org/0000-0003-0374-2168

Complete contact information is available at:
https://pubs.acs.org/10.1021/acs.nanolett.1c01562

Author Contributions

All authors were involved in designing the research, performing the research, and writing the paper.

Notes

The authors declare no competing financial interest.

REFERENCES

(1) Basov, D. N.; Fogler, M. M.; Garcia de Abajo, F. J. Polaritons in van der Waals materials. *Science* **2016**, *354*, aag1992.

(2) Low, T.; et al. Polaritons in layered two-dimensional materials. *Nat. Mater.* **2017**, *16*, 182−194.

(3) Caldwell, J. D.; Lindsay, L.; Giannini, V.; Vurgaftman, I.; Reinecke, T. L.; Maier, S. A.; Glembocki, O. J.; et al. Low-loss, infrared and terahertz nanophotonics using surface phonon polaritons. *Nanophotonics* **2015**, *4*, 44.

(4) Dai, S.; et al. Tunable phonon polaritons in atomically thin van der Waals crystals of boron nitride. *Science* **2014**, *343*, 1125−1129.

(5) Li, P.; Lewin, M.; Kretinin, A. V.; Caldwell, J. D.; Novoselov, K. S.; Taniguchi, T.; Watanabe, K.; Gaussmann, F.; Taubner, T. Hyperbolic phonon-polaritons in boron nitride for near-field optical imaging and focusing. *Nat. Commun.* **2015**, *6*, 1−9.

(6) Giles, A. J.; et al. Ultralow-loss polaritons in isotopically pure boron nitride. *Nat. Mater.* **2018**, *17*, 134−139.

(7) Basov, D. N.; Asenjo-Garcia, A.; Schuck, P. J.; Zhu, X. Y.; Rubio, A. Polaritons Panorama. *Nanophotonics* **2020**, *10*, 549.

(8) Ni, G. X.; et al. Fundamental limits to graphene plasmonics. *Nature* **2018**, *557*, 530−533.

(9) Jiang, B.-Y.; Ni, G.-X.; Addison, Z.; Shi, J. K.; Liu, X.; Zhao, S. Y. F.; Kim, P.; Mele, E. J.; Basov, D. N.; Fogler, M. M. Plasmon reflections by topological electronic boundaries in bilayer graphene. *Nano Lett.* **2017**, *17*, 7080−7085.

(10) Ni, G. X.; et al. Plasmons in graphene moiré superlattices. *Nat. Mater.* **2015**, *14*, 1217−1222.

(11) Goldflam, M. D.; Ni, G.-X.; Post, K. W.; Fei, Z.; Yeo, Y.; Tan, J. Y.; Rodin, A. S.; Chapler, B. C.; Ozyilmaz, B.; Castro Neto, A. H.; Fogler, M. M.; Basov, D. N. Tuning and persistent switching of graphene plasmons on a ferroelectric substrate. *Nano Lett.* **2015**, *15*, 4859−4864.

(12) Sunku, S. S.; et al. Photonic crystals for nano-light in moire graphene superlattices. *Science* **2018**, *362*, 1153−1156.

(13) Fei, Z.; Ni, G.-X.; Jiang, B.-Y.; Fogler, M. M.; Basov, D. N. Nanoplasmonics phenomena at electronic boundaries in graphene. *ACS Photonics* **2017**, *4*, 2971−2977.

(14) Ma, W.; et al. In-plane anisotropic and ultra-low-loss polaritons in a natural van der Waals crystal. *Nature* **2018**, *562*, 557−562.

(15) Zheng, Z.; et al. A mid-infrared biaxial hyperbolic van der Waals crystal. *Science Adv.* **2019**, *5*, eaav8690.

(16) Hu, G.; et al. Topological polaritons and photonic magic angles in twisted α-MoO$_3$ bilayers. *Nature* **2020**, *582*, 209−213.

(17) Zheng, Z.; Chen, J.; Wang, Y.; Wang, X.; Chen, X.; Liu, P.; Xu, J.; Xie, W.; Chen, H.; Deng, S.; Xu, N. Highly confined and tunable hyperbolic phonon polaritons in van der Waals semiconducting transition metal oxides. *Adv. Mater.* **2018**, *30*, 1705318.

(18) Chen, M.; et al. Configurable phonon polaritons in twisted α-MoO$_3$. *Nat. Mater.* **2020**, *19*, 1307−1311.

(19) Duan, J.; et al. Twisted nano-optics: manipulating light at the nanoscale with twisted phonon polariton slabs. *Nano Lett.* **2020**, *20*, 5323−5329.

(20) McLeod, A. S.; et al. Nanotextured phase coexistence in the correlated insulator V$_2$O$_3$. *Nat. Phys.* **2017**, *13*, 80−86.

(21) McLeod, A. S.; et al. Multi-messenger nanoprobes of hidden magnetism in a strained magnanite. *Nat. Mater.* **2020**, *19*, 397−404.

(22) Post, K. W.; et al. Coexisting first- and second-order electronic phase transitions in a correlated oxide. *Nat. Phys.* **2018**, *14*, 1056−1061.

(23) Ni, G. X.; et al. Ultrafast optical switching of infrared plasmon polaritons in high-mobility graphene. *Nat. Photonics* **2016**, *10*, 244−247.

(24) Ni, G. X.; Wang, H.; Jiang, B.-Y.; Chen, L. X.; Du, Y.; Sun, Z. Y.; Goldflam, M. D.; Frenzel, A. J.; Xie, X. M.; Fogler, M. M.; Basov, D. N.; et al. Soliton superlattices in twisted hexagonal boron nitride. *Nat. Commun.* **2019**, *10*, 1−6.

(25) Berkowitz, M. E.; et al. Hyperbolic cooper-pair polaritons in planar graphene/cuprate plasmonic cavities. *Nano Lett.* **2021**, *21*, 308−316.

(26) Tamagnone, M.; Ambrosio, A.; Chaudhary, K.; Jauregui, L. A.; Kim, P.; Wilson, W. L.; Capasso, F. Ultra-confined mid-infrared resonant phonon polaritons in van der Waals nanostructures. *Science Adv.* **2018**, *4*, eaat7189.

(27) Fali, A.; et al. Refractive index-based control of hyperbolic phonon polariton propagation. *Nano Lett.* **2019**, *19*, 7725−7734.

(28) Segura, A.; Cuscó, R.; Taniguchi, T.; Watanabe, K.; Artús, L. Long lifetime of the E1u in-plane infrared-active modes of h-BN. *Phys. Rev. B: Condens. Matter Mater. Phys.* **2020**, *101*, 235203.

(29) Cuscó, R.; Gil, B.; Cassabois, G.; Artús, L. Temperature dependence of Raman-active phonons and anharmonic interactions in layered hexagonal BN. *Phys. Rev. B: Condens. Matter Mater. Phys.* **2016**, *94*, 155435.

(30) Stupakiewicz, A. Ultrafast phononic switching of magnetization. *Nat. Phys.* **2021**, *17*, 489.

(31) Sun, Z.; Gutierrez-Rubio, A.; Basov, D. N.; Fogler, M. M. Hamiltonian optics of hyperbolic polaritons in nanogranules. *Nano Lett.* **2015**, *15*, 4455−4460.

(32) Gu, M.; Rondinelli, M. Nonlinear phonic control and emergent magnetism in Mott insulating titanates. *Phys. Rev. B: Condens. Matter Mater. Phys.* **2018**, *98*, 024102.